

Disrupted Calcium Release as a Mechanism for Atrial Alternans Associated with Human Atrial Fibrillation

Kelly C. Chang¹, Jason D. Bayer², Natalia A. Trayanova^{1*}

1 Institute for Computational Medicine, Department of Biomedical Engineering, Johns Hopkins University, Baltimore, Maryland, United States of America, **2** IHU-LIRYC - L'Institut de Rythmologie et Modélisation Cardiaque, University of Bordeaux, Bordeaux, France



Abstract

Atrial fibrillation (AF) is the most common cardiac arrhythmia, but our knowledge of the arrhythmogenic substrate is incomplete. Alternans, the beat-to-beat alternation in the shape of cardiac electrical signals, typically occurs at fast heart rates and leads to arrhythmia. However, atrial alternans have been observed at slower pacing rates in AF patients than in controls, suggesting that increased vulnerability to arrhythmia in AF patients may be due to the proarrhythmic influence of alternans at these slower rates. As such, alternans may present a useful therapeutic target for the treatment and prevention of AF, but the mechanism underlying alternans occurrence in AF patients at heart rates near rest is unknown. The goal of this study was to determine how cellular changes that occur in human AF affect the appearance of alternans at heart rates near rest. To achieve this, we developed a computational model of human atrial tissue incorporating electrophysiological remodeling associated with chronic AF (cAF) and performed parameter sensitivity analysis of ionic model parameters to determine which cellular changes led to alternans. Of the 20 parameters tested, only decreasing the ryanodine receptor (RyR) inactivation rate constant (k_{iCa}) produced action potential duration (APD) alternans seen clinically at slower pacing rates. Using single-cell clamps of voltage, fluxes, and state variables, we determined that alternans onset was Ca^{2+} -driven rather than voltage-driven and occurred as a result of decreased RyR inactivation which led to increased steepness of the sarcoplasmic reticulum (SR) Ca^{2+} release slope. Iterated map analysis revealed that because SR Ca^{2+} uptake efficiency was much higher in control atrial cells than in cAF cells, drastic reductions in k_{iCa} were required to produce alternans at comparable pacing rates in control atrial cells. These findings suggest that RyR kinetics may play a critical role in altered Ca^{2+} homeostasis which drives proarrhythmic APD alternans in patients with AF.

Citation: Chang KC, Bayer JD, Trayanova NA (2014) Disrupted Calcium Release as a Mechanism for Atrial Alternans Associated with Human Atrial Fibrillation. *PLoS Comput Biol* 10(12): e1004011. doi:10.1371/journal.pcbi.1004011

Editor: Andrew D. McCulloch, University of California San Diego, United States of America

Received: May 27, 2014; **Accepted:** October 29, 2014; **Published:** December 11, 2014

Copyright: © 2014 Chang et al. This is an open-access article distributed under the terms of the Creative Commons Attribution License, which permits unrestricted use, distribution, and reproduction in any medium, provided the original author and source are credited.

Data Availability: The authors confirm that all data underlying the findings are fully available without restriction. Parameter files, model files, and example scripts used to run the simulations presented in the paper can be found on FigShare. <http://dx.doi.org/10.6084/m9.figshare.1201512>.

Funding: This research was supported by National Institutes of Health grant DP1-HL123271 (<http://www.nih.gov>), the David C. Gakenheimer Fellowship, an ARCS/MWC Scholar Award from the KPMG Foundation (<http://www.arcsfoundation.org>), and a scholarship from the Whitaker International Program (<http://www.whitaker.org/>). The funders had no role in study design, data collection and analysis, decision to publish, or preparation of the manuscript.

Competing Interests: I have read the journal's policy and the authors of this manuscript have the following competing interests: Natalia A. Trayanova is a cofounder of CardioSolv, LLC. CardioSolv was not involved in this research.

* Email: ntrayanova@jhu.edu

Introduction

Atrial fibrillation (AF) is currently the most common cardiac rhythm disorder, posing a significant medical and economic challenge for the US health care system [1,2]. This burden is likely to increase as the population ages and AF prevalence rises [3]. Effective prevention and treatment of AF depends upon advances in our understanding of underlying disease mechanisms. Although several features of AF electrophysiological remodeling have been identified over the past decades [4,5], our knowledge about the arrhythmogenic substrate remains incomplete.

Beat-to-beat alternation in the shape of cardiac electrical signals, a phenomenon called alternans, has been observed in the atria of AF patients, but the mechanism underlying these alternans is not known [6–11]. Narayan *et al.* reported differences in the rate dependence of action potential duration (APD) alternans in patients, with APD alternans occurring at pacing rates near rest in AF patients but only at fast pacing rates in controls [8]. Narayan *et al.* also found that APD alternans always

preceded AF initiation, indicating that alternans may play an important role in establishing the arrhythmogenic substrate and creating vulnerability to AF. Thus, a better understanding of AF arrhythmogenesis will likely depend upon identification of the mechanism driving atrial alternans at heart rates near rest.

Interestingly, in AF patients the slope of the APD restitution curve was <1 during APD alternans onset at slow pacing rates. This suggests that a cellular mechanism other than voltage-driven instability underlies APD alternans at heart rates near rest [9]. Altered Ca^{2+} handling in atrial myocytes is known to play a crucial role in the generation of AF triggers and in AF maintenance [12,13]. Ca^{2+} cycling instabilities have been shown to underlie ventricular alternans in heart failure [14,15], as well as atrial alternans in several non-AF animal models [16–18]. However, it is unknown whether these represent a plausible mechanism for atrial alternans in AF patients, particularly at heart rates near rest. We therefore sought to determine, using a computer model of human atrial tissue, whether Ca^{2+} handling abnormalities, or other electrophysiological changes that occur in AF, lead to APD

Author Summary

Atrial fibrillation is an irregular heart rhythm affecting millions of people worldwide. Effective treatment of this cardiac disorder relies upon our detailed knowledge and understanding of the mechanisms that lead to arrhythmia. Recent clinical observations have suggested that alternans, a phenomenon where the shape of the electrical signal in the heart alternates from beat to beat, may play an important role in this process, but the underlying mechanisms remain unknown. In this study, we use computational models to conduct a detailed examination of the causes and contributors to alternans associated with human atrial fibrillation. We find that in atria remodeled by atrial fibrillation, alternans appears near resting heart rates because several aspects of calcium cycling are disrupted in the atrial cells. In particular, the release and uptake of calcium from the cellular storage compartment, the sarcoplasmic reticulum, becomes imbalanced, leading to alternation in calcium signals from beat to beat. These findings provide important insights into the mechanisms of proarrhythmic alternans in human atrial fibrillation which may be used to develop novel therapeutic targets and treatment strategies in the future.

alternans. We identified a critical change in the kinetics of the ryanodine receptor (RyR) that was responsible for APD alternans onset at slower pacing rates, and subsequently aimed to elucidate the mechanistic relationship between this disruption in RyR kinetics and alternans onset. To this end, we employed single-cell clamping of ionic model parameters and iterated map analysis in order to dissect the mechanisms which drive alternans in atrial tissue, as well as to provide important insights into the pathophysiological changes that contribute to the development of alternans in AF patients.

Results

APD alternans in the human AF tissue model

In order to investigate ionic mechanisms in human AF that contribute to the generation of atrial APD alternans at the tissue level, we created a computer model of human atrial tissue incorporating ionic remodeling associated with chronic AF (cAF), as described in Methods. The sensitivity of APD alternans to ionic model parameters was evaluated by varying parameters one at a time and applying the clinical pacing protocol used by Narayan *et al.* to induce APD alternans in AF patients [8] (see Table 1 and Methods). For control, a model of normal human atrial tissue was also simulated. We then assessed the magnitude and onset pacing cycle length (CL) of APD alternans by analyzing voltage traces from the recording electrode (Fig. 1A), as outlined in Methods.

In the control model, significant APD alternans did not occur before loss of capture at 260 ms CL (Fig. 1B). However, in the cAF-remodeled tissue preparation, significant APD alternans appeared at a CL of 240 ms (Fig. 1B). Varying the RyR inactivation rate constant (ki_{Ca}) had the greatest effect on alternans onset CL in the human cAF-remodeled tissue (Fig. 2A). In fact, only reduction of ki_{Ca} resulted in alternans onset at CLs of 300–500 ms (Fig. 2B), matching alternans onset CLs observed in AF patients [8]. When other ionic model parameters were varied from their original cAF values, APD alternans either did not appear in the tissue model at $CL \geq 300$ ms (Fig. 2A, blue areas), appeared only at $CL \leq 350$ ms (Fig. 2A, red areas), or did not appear before loss of capture or conduction block occurred in the tissue (Fig. 2A,

white spaces). These results suggest that altered RyR kinetics is the critical cellular component underlying the occurrence of APD alternans in AF patients at pacing rates near rest, and that ki_{Ca} plays a key role in this process.

We also tested whether differences between left and right atrial electrophysiology affect alternans susceptibility using a right atrium (RA) version of the cAF model [19] in tissue simulations. Results for RA tissue were very similar to those for the left atrium (LA), demonstrating that modulation of ki_{Ca} could reproduce alternans observed at pacing rates near rest in both the LA and RA of AF patients [8] (S2 Figure).

When ki_{Ca} was decreased by 50% in the cAF model (we refer to this as the cAF_{alt} ionic model), APD alternans onset data from the human AF tissue model agreed well with data from persistent AF patients. Significant APD alternans began at 400-ms CL (Fig. 1B, dotted red line), mean APD at onset was 229 ms, and APD alternans magnitude at onset was 27 ms (Fig. 1C, dotted red line). These metrics were each within one standard deviation (SD) of clinical observations [8] (Fig. 3). The cAF_{alt} model also displayed noticeable alternans in intracellular Ca^{2+} ($[Ca^{2+}]_i$) at the onset CL (Fig. 1D). For both the cAF and cAF_{alt} models, mean APDs were shorter than in the control model (Fig. 1B–C), and diastolic and systolic $[Ca^{2+}]_i$ were lower than in control (Fig. 1D). At 400-ms CL in the cAF_{alt} model, on the odd (long) vs. the even (short) beat (Fig. 4, blue vs. red), there was higher sarcoplasmic reticulum (SR) Ca^{2+} load before release (0.288 vs. 0.273 mM), higher peak RyR open probability (RyR_o) ($9.0e-4$ vs. $4.7e-4$), a larger intracellular Ca^{2+} transient (CaT) amplitude ($\Delta[Ca^{2+}]_i = 0.13$ vs. $0.067 \mu M$), similar L-type Ca^{2+} (LCC) current (integrated over one beat: 144 vs. 140 mC/F), and increased Na^+ / Ca^{2+} exchanger (NCX) current (I_{NCX} , integrated over one beat: 98.4 vs. 74.5 mC/F). The positive coupling between transmembrane potential (V_m) and Ca^{2+} , with I_{NCX} as the primary electrogenic current, is consistent with experimental findings [20]. Since the magnitude and onset of APD alternans in the cAF_{alt} model provided the best agreement with clinical APD alternans data (Fig. 3), we chose to use this model for subsequent investigations into the underlying causes of alternans occurrence.

SR Ca^{2+} release underlies alternans onset

Since APD alternans throughout the homogenous cAF_{alt} tissue preparation were concordant and of similar magnitude (S3 Figure), electrotonic effects and CV restitution were excluded as factors influencing these alternans. Indeed, APD and CaT alternans in the cAF_{alt} tissue model were very similar to alternans in the isolated single-cell cAF_{alt} model (Fig. 5, left column vs. Fig. 4, top row). We therefore concluded that cellular mechanisms gave rise to alternans in the cAF_{alt} tissue model and decided to utilize single-cell simulations in order to investigate these mechanisms. We first used the ionic model variable clamping protocol described in detail in Methods. The percent change in APD and CaT alternans magnitudes, when each ionic model variable was clamped to its trace from either the even (short) or odd (long) steady-state beat at the alternans onset CL (400 ms), are summarized in Fig. 6 (right column: state variables, left column: currents and fluxes). Variables which resulted in $>99\%$ reduction in APD and CaT alternans magnitudes for both even and odd beat clamps were considered essential for alternans.

Clamping V_m resulted in -61.8% change in CaT alternans magnitude for even beat clamps and $+6.6\%$ for odd beat clamps, demonstrating that the alternans were not voltage-driven (see even and odd beat clamps depicted in column 2 of Fig. 5 and S4 Figure, respectively). Clamping $[Ca^{2+}]_i$ enhanced APD alternans ($+55.2\%$ and $+75.8\%$ for even and odd beat clamps, respectively, column 3

Table 1. Ionic model parameters used in parameter sensitivity analysis.

Parameter	Description
g_{Na}	Maximal fast Na^+ current conductance
g_{NaL}	Maximal late Na^+ current conductance
g_{CaL}	Maximal L-type Ca^{2+} current conductance
τ_f	L-type Ca^{2+} current voltage-dependent inactivation time constant
τ_{fCa}	Maximal L-type Ca^{2+} current calcium-dependent inactivation time constant
g_{K1}	Maximal inward rectifier K^+ current conductance
g_{Kr}	Maximal rapidly activating delayed rectifier K^+ current conductance
g_{Ks}	Maximal slowly activating delayed rectifier K^+ current conductance
g_{Kur}	Maximal ultrarapid delayed rectifier K^+ current conductance
g_{to}	Maximal transient outward K^+ current conductance
$I_{bar_{NCX}}$	Maximal Na^+/Ca^{2+} exchanger current
k_s	SR Ca^{2+} release rate constant
k_{im}	Transition rate constant for the RyR
k_{om}	Transition rate constant for the RyR
k_{iCa}	Baseline inactivation rate constant for the RyR without luminal SR Ca^{2+} dependence
k_{oCa}	Baseline activation rate constant for the RyR without luminal SR Ca^{2+} dependence
k_{leak}	SR Ca^{2+} leak rate constant
$V_{maxSRCaP}$	V_{max} of SERCA pump
EC_{50SR}	EC_{50} for luminal Ca^{2+} dependence of the RyR
K_{mf}	K_m for SERCA pump in forward mode

doi:10.1371/journal.pcbi.1004011.t001

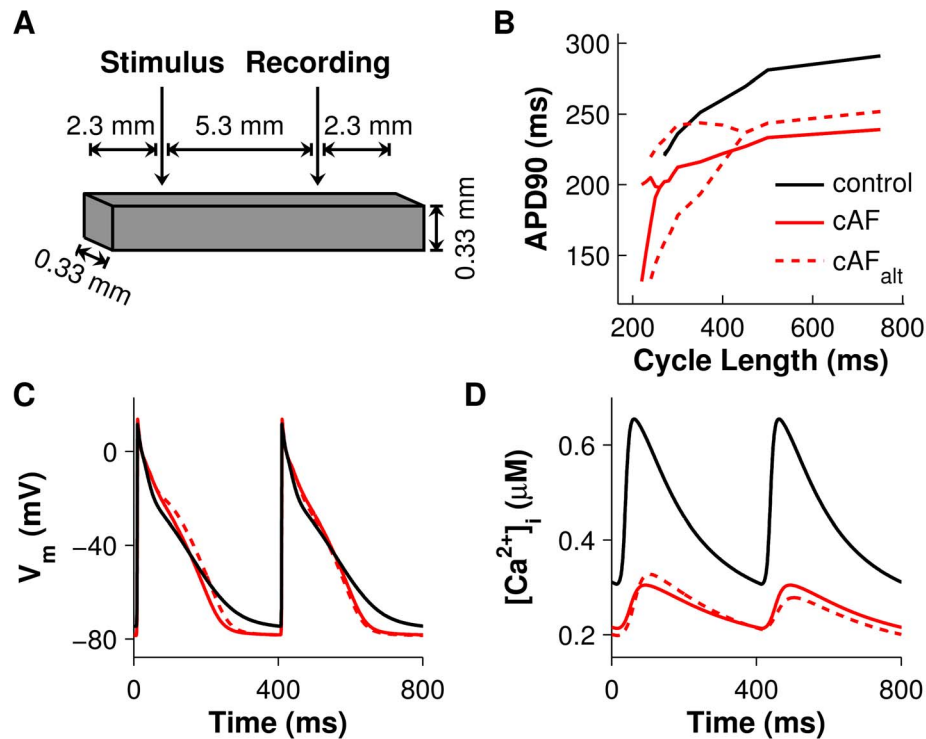


Fig. 1. Tissue preparation setup and comparisons of control, cAF, and cAF_{alt} tissue during pacing. (A) Atrial tissue mesh with stimulus and recording electrodes. (B) APD restitution curves for control tissue (black), cAF-remodeled tissue [19] (red), and cAF_{alt} tissue with APD alternans onset and amplitude matching clinical data [8] (dotted red line). The RyR inactivation rate constant (k_{iCa}) was reduced 50% in the cAF model to create the cAF_{alt} model. APs (C) and CaTs (D) recorded from the last two beats at 400-ms pacing CL. Alternans are present in the cAF_{alt} tissue but not in control or cAF tissue.

doi:10.1371/journal.pcbi.1004011.g001

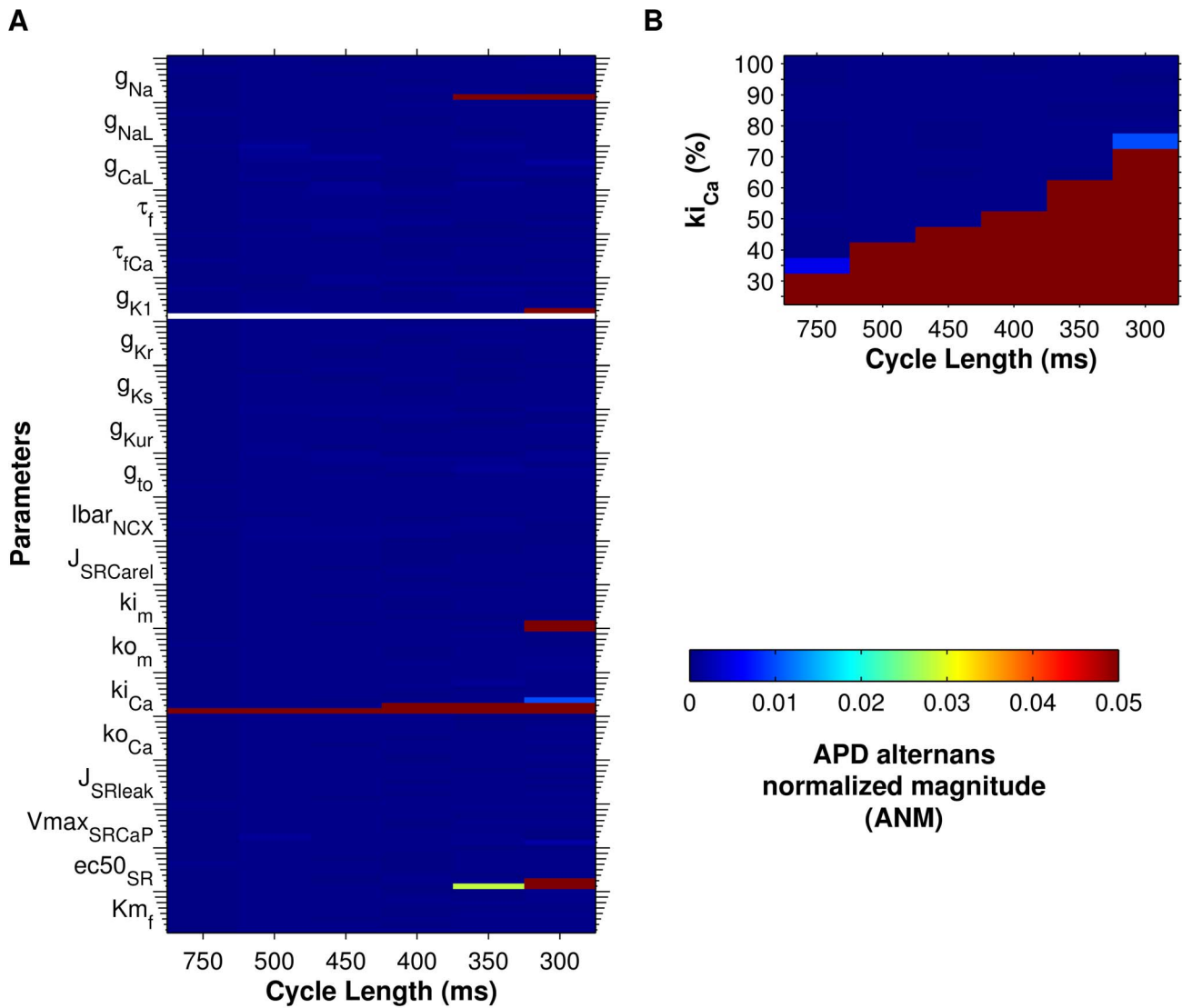


Fig. 2. Sensitivity of APD alternans magnitude to ionic model parameters in cAF tissue. Parameter sensitivity analysis was performed in cAF tissue in order to identify ionic model parameters that influence alternans. For panels A and B, APD alternans normalized magnitude (ANM) is indicated by the colorbar (>0.05 considered significant). (A) Parameters were scaled one at a time between 25% (short ticks) and 200% (long ticks) of their AF model values (25% increments). Only decreasing the RyR inactivation rate constant (k_{iCa}) produced alternans at the longest CLs. (B) k_{iCa} was scaled between 25% and 100% in 5% increments, producing a range of APD alternans onset CLs between 300–750 ms. doi:10.1371/journal.pcbi.1004011.g002

of Fig. 5 and S4 Figure). However, when SR Ca^{2+} ($[Ca^{2+}]_{SR}$) was clamped to either the even or odd beat waveforms, alternans in both APD and CaT were eliminated ($<-99\%$), demonstrating that the alternans were driven by SR Ca^{2+} instability (column 4 of Fig. 5 and S4 Figure). In addition, four other variables could be clamped to the even or odd beat waveforms to eliminate APD and CaT alternans: RyR inactivated probability (RyR_i), RyR open probability (RyR_o), junctional Ca^{2+} ($[Ca^{2+}]_j$), and SR Ca^{2+} release flux ($J_{SRCarel}$) (Fig. 6, and S5 and S6 Figures). All five of these variables were therefore critical for enabling alternans to occur at the onset CL. Furthermore, these variables directly impact SR Ca^{2+} release, implicating SR Ca^{2+} release as the underlying source of alternans in the cAF_{alt} model.

There were two ionic model components which greatly reduced but did not eliminate alternans when clamped: sub-sarcolemmal Ca^{2+} ($[Ca^{2+}]_sl$) and sub-sarcolemmal Na^+/Ca^{2+} exchanger current (I_{NCXsl}). Clamping $[Ca^{2+}]_sl$ to the even beat eliminated all

alternans; clamping to the odd beat greatly reduced APD and CaT alternans (-95.8% and -96.2% , respectively), although large alternation in SR load persisted (Fig. 6 and columns 1–2 of S7 Figure). Similarly, clamping I_{NCXsl} to the even beat waveform resulted in elimination of APD but not CaT alternans ($+72.9\%$), while clamping to the odd beat waveform resulted in elimination of all alternans (Fig. 6 and columns 3–4 of S7 Figure). Hence, the SR Ca^{2+} -driven instabilities produced alternans in Ca^{2+} cycling which were positively coupled to voltage through I_{NCXsl} and $[Ca^{2+}]_sl$.

Steepening of the SR Ca^{2+} release slope results in alternans

Increased steepness of the SR release-load relationship is a well-known mechanism for CaT alternans [21,22]. The importance of SR Ca^{2+} release variables for APD and CaT alternans, as demonstrated by the results in Fig. 5, 6, and S4, S5, S6 Figures,

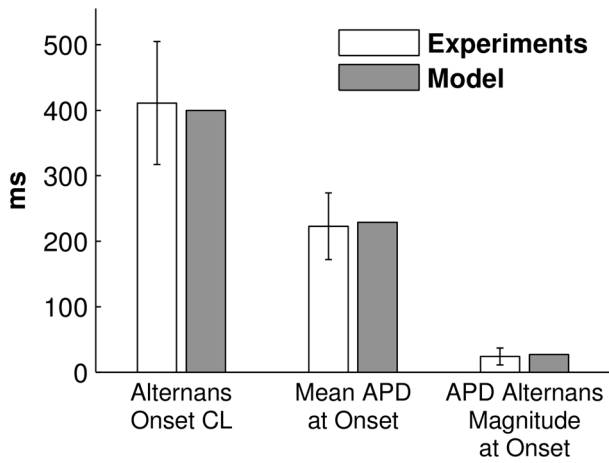


Fig. 3. Comparison of alternans onset characteristics in persistent AF patients and in the cAF_{alt} tissue model. Mean±SD alternans onset data during pacing in persistent AF patients (white bars) was taken from Table 2 in Ref. [8]. When the cAF_{alt} tissue model was paced similarly, alternans onset CL, mean APD at onset, and APD alternans magnitude at onset were within one SD of clinical data (gray bars). doi:10.1371/journal.pcbi.1004011.g003

led us to hypothesize that such a mechanism might give rise to Ca²⁺-driven alternans in the cAF_{alt} model at pacing rates near rest. To test this, we compared the cAF and cAF_{alt} ionic models under action potential (AP) voltage clamp conditions so that changes in CaT alternans would be due solely to changes in Ca²⁺ homeostasis rather than bidirectional coupling between V_m and Ca²⁺. After clamping each ionic model at a CL of 400 ms until steady state was reached, we perturbed [Ca²⁺]_{SR} and tracked SR load and SR Ca²⁺ release on the subsequent clamped beats (see Methods for details). The SR release-load relationships for the cAF (black) and cAF_{alt} (red) ionic models are depicted in Fig. 7 (left column, row 1). The slope of the release-load relationship in the cAF_{alt} model (*m* = 3.1) was much greater than the slope in the cAF model (*m* = 1.7), confirming our hypothesis that differences between the

cAF and cAF_{alt} ionic models led to a steepening of the SR Ca²⁺ release slope.

To better explain the differences between the cAF and cAF_{alt} ionic models that gave rise to different SR Ca²⁺ release slopes, we first compared [Ca²⁺]_{SR}, RyR_o, [Ca²⁺]_j, and cumulative Ca²⁺ release for the two models at steady state (Fig. 7, left column, rows 2–5, solid lines). In the cAF_{alt} model, [Ca²⁺]_{SR} at steady state was 19.7% lower than in the cAF model as a result of increased RyR opening (Fig. 7, left column, rows 2 and 3, red vs. black solid lines). Although this led to a 15.2% decrease in peak [Ca²⁺]_j in the cAF_{alt} model, the duration of the release event was prolonged (Fig. 7, left column, row 4, red vs. black solid lines). Consequently, though cumulative Ca²⁺ release in the cAF_{alt} model initially lagged behind, at *t* ≈ 90 ms it actually surpassed the cumulative release in the cAF model, ultimately resulting in a 3.4% increase in total release by the end of the beat (Fig. 7, left column, row 5, red vs. black solid lines).

To illustrate how these differences between the cAF and cAF_{alt} ionic models impacted SR release slope, we applied a large perturbation to [Ca²⁺]_{SR} (+20 μM) at the beginning of a clamped beat and compared the unperturbed (steady state, solid line) and perturbed (dotted line) traces for each model (Fig. 7, left column, rows 2–6). Higher SR load at the beginning of the beat led to increased SR release flux due to luminal Ca²⁺ regulation of the RyR (causing more opening), as well as to the increased concentration gradient between the SR and junctional compartments. In both the cAF and cAF_{alt} models, these changes led to increased peak [Ca²⁺]_j (+54.4% and +100%, respectively) and RyR opening (+64.6% and +129%, respectively) as a result of more Ca²⁺-induced Ca²⁺ release (Fig. 7, left column, rows 2–4). The positive feedback relationship between [Ca²⁺]_j and RyR opening was strong enough such that when SR load was increased (Fig. 7, left column, row 2, dotted vs. solid lines), this actually resulted in a lower minimum [Ca²⁺]_{SR} during release (−3.6% and −13.3% for cAF and cAF_{alt} models, respectively). However, the amount of positive feedback differed between the cAF and cAF_{alt} ionic models. Positive feedback amplifies changes in release inputs, such as SR load; therefore, in the cAF model, where [Ca²⁺]_j is higher and positive feedback is stronger, the increase in [Ca²⁺]_{SR} produced a slightly greater change in release (compared to the

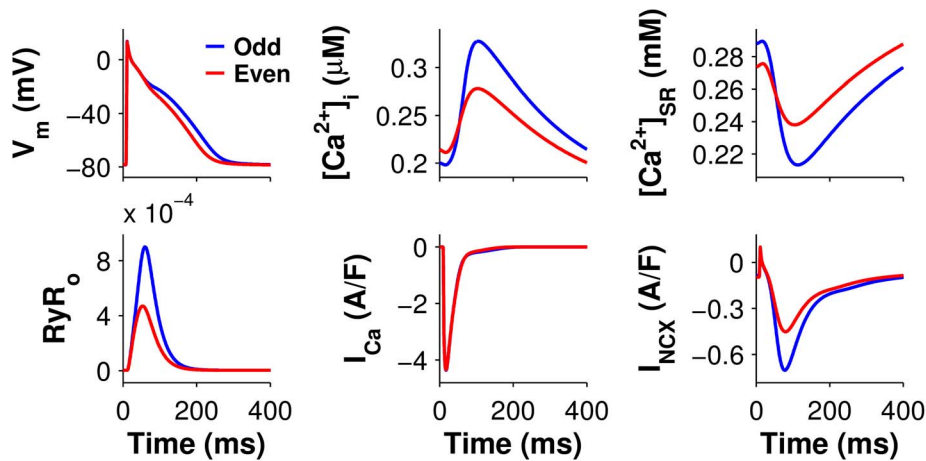


Fig. 4. Alternans in cAF_{alt} tissue at the onset CL. The odd (blue) and even (red) beats at the alternans onset CL (400 ms) are shown superimposed. Large Ca²⁺ release occurred during the long beat (blue traces). Top (left to right): transmembrane potential (V_m), intracellular Ca²⁺ ([Ca²⁺]_j), and SR Ca²⁺ concentration ([Ca²⁺]_{SR}). Bottom (left to right): RyR open probability (RyR_o), L-type Ca²⁺ current (I_{Ca}), Na⁺/Ca²⁺ exchanger current (I_{NCX}). doi:10.1371/journal.pcbi.1004011.g004

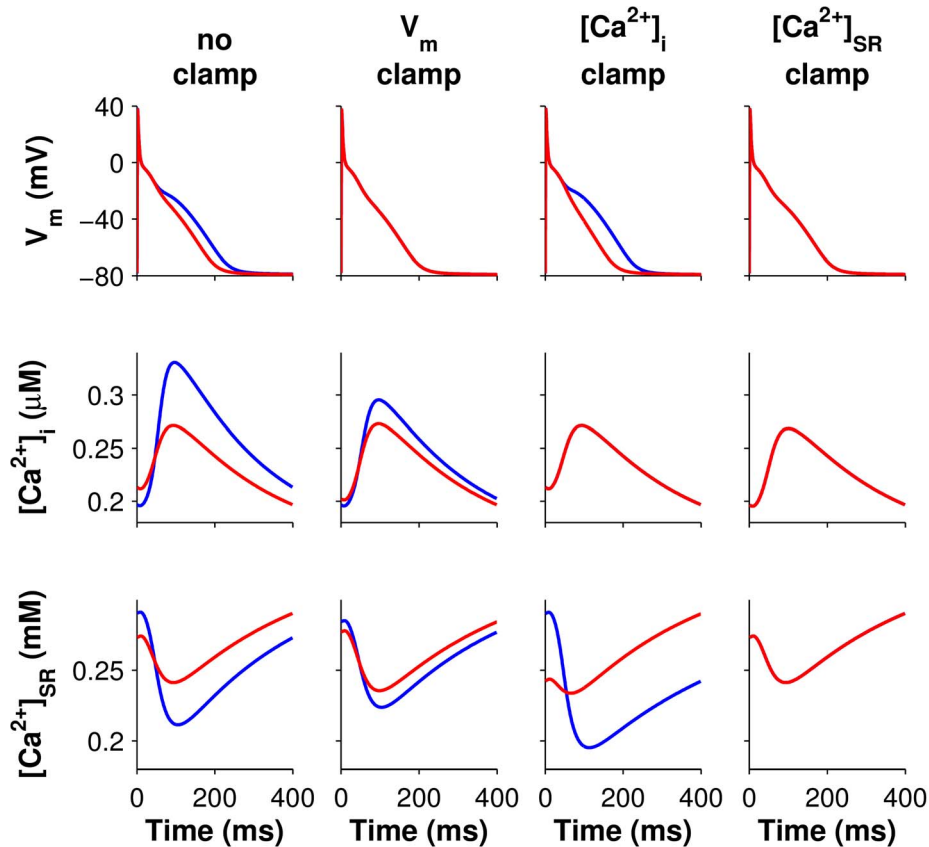


Fig. 5. Voltage and Ca^{2+} even beat clamps for the single-cell cAF_{alt} model. Traces of transmembrane potential (V_m , row 1), intracellular Ca^{2+} ($[\text{Ca}^{2+}]_i$, row 2), and SR Ca^{2+} ($[\text{Ca}^{2+}]_{\text{SR}}$, row 3) from two consecutive beats are superimposed to show alternans between even (red) and odd (blue) beats. Column 1: the unclamped cAF_{alt} cell paced to steady state at 400-ms CL displayed alternans in V_m and Ca^{2+} . The red traces depicted in column 1 were used to clamp V_m (column 2), $[\text{Ca}^{2+}]_i$ (column 3), or $[\text{Ca}^{2+}]_{\text{SR}}$ (column 4). Alternans persisted when V_m or $[\text{Ca}^{2+}]_i$ is clamped, but clamping $[\text{Ca}^{2+}]_{\text{SR}}$ eliminated alternans.

doi:10.1371/journal.pcbi.1004011.g005

unperturbed, steady state simulation) during the rising phase of $[\text{Ca}^{2+}]_j$ ($t < 48$ ms) than in the cAF_{alt} model (Fig. 7, left column, row 6, black vs. red).

By contrast, termination of release occurs through a negative feedback process, with RyRs inactivating upon the binding of junctional Ca^{2+} . Negative feedback attenuates changes in release so that robust, fast termination of release is achieved even when a disturbance (such as a transient increase in SR load) occurs. In the cAF_{alt} model, negative feedback is decreased both directly, via reduction of $k_{\text{Ca}^{2+}}$, and indirectly, via reduction in $[\text{Ca}^{2+}]_j$ that occurs as a result of decreased SR load. This causes prolongation of the Ca^{2+} release event and a larger peak $[\text{Ca}^{2+}]_j$ (Fig. 7, left column, row 4, red vs. black dotted lines). Consequently, when SR load was increased by the same amount in the cAF and cAF_{alt} models, although the cAF_{alt} model had a lesser initial change in release because of weaker positive feedback, it also had a greater final change in release, i.e. a steeper SR release-load relationship, because of weaker negative feedback (Fig. 7, left column, row 6, red vs. black).

The results in column 1 of Fig. 7 demonstrate how the steeper SR release slope in the cAF_{alt} ionic model (as compared to the cAF ionic model) depends upon RyR inactivation by junctional Ca^{2+} . However, recent work suggests that termination of release does not rely on direct Ca^{2+} -dependent inactivation of the RyR but rather on local SR Ca^{2+} depletion [23–26]. In order to test whether steepening of the SR release slope could occur in the cAF model

by an alternative release termination mechanism, we implemented a version of the cAF model in which the RyR Markov model was replaced with that of Sato and Bers and the SR was divided into junctional (JSR) and network (NSR) compartments [27] (see Table 2 and S1 Text). Termination of release in this alternative RyR model relies on calsequestrin (CSQN) binding to the RyR, which occurs as luminal $[\text{Ca}^{2+}]$ decreases causing changes in RyR opening and closing rates.

The effects of decreased RyR termination in the Sato-Bers RyR model are shown in the right column of Fig. 7. When the CSQN-bound RyR closing rate k_{34} (analogous to the inactivation rate $k_{\text{Ca}^{2+}}$ in the original model) is decreased from 100% to 50% (cAF_{alt}), steady-state Ca^{2+} concentrations change modestly as compared to the original RyR formulation (Fig. 7, black vs. red solid lines), but nevertheless display similar trends: $[\text{Ca}^{2+}]_{\text{JSR}}$ decreases by 1.5% (vs. 19.7%, row 2), peak $[\text{Ca}^{2+}]_j$ is reduced by 10.5% (vs. 15.2%, row 4) and delayed, and total release increases by 3.6% (vs. 3.4%, row 5). When $[\text{Ca}^{2+}]_{\text{NSR}}$ is perturbed in the Sato-Bers models by +20 μM , Ca^{2+} release increases more in the cAF_{alt} model than in the cAF model (Fig. 7, right column, row 6, red vs. black dotted lines). Consequently, the SR Ca^{2+} release slope is steeper in the cAF_{alt} model ($m = 3.7$ vs 1.9, Fig. 7, right column, row 1). Thus, although changes in SR Ca^{2+} release slope in the original cAF model are caused by altered junctional Ca^{2+} -dependent inactivation, altered SR Ca^{2+} -dependent mechanisms of release termination can produce such changes in SR Ca^{2+} release slope as well.

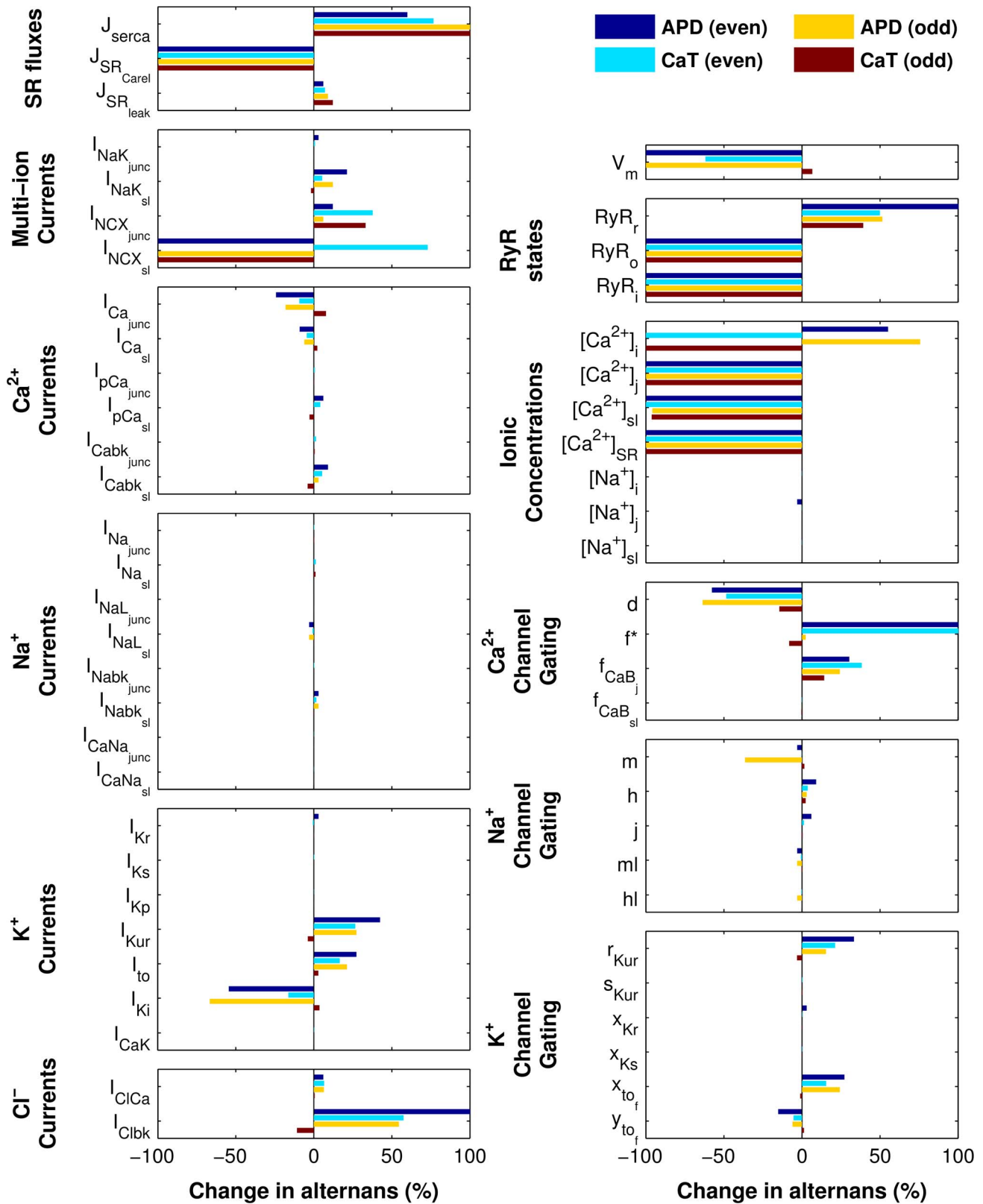


Fig. 6. Summary of ionic model variable clamps for the single-cell cAF_{ait} model. Results for all ionic model variable clamping simulations are summarized in bar graphs showing the percent changes in APD and CaT alternans magnitudes when model variables were clamped to even or odd beat waveforms. Alternans were eliminated (>99% decrease in APD and CaT alternans magnitudes for both even and odd beat waveforms) only when SR release variables were clamped (SR Ca²⁺ release flux, J_{SRCarel}; RyR open probability, RyR_o; RyR inactivated probability, RyR_i; SR Ca²⁺ ([Ca²⁺]_{SR}); and junctional Ca²⁺ ([Ca²⁺]_j). Gating variable f (asterisk) displayed higher order instability when clamping to the even beat waveform, so the increase in alternans magnitude was considered infinitely large. Left column: SR fluxes and sarcolemmal currents. Right column: state variables.
doi:10.1371/journal.pcbi.1004011.g006

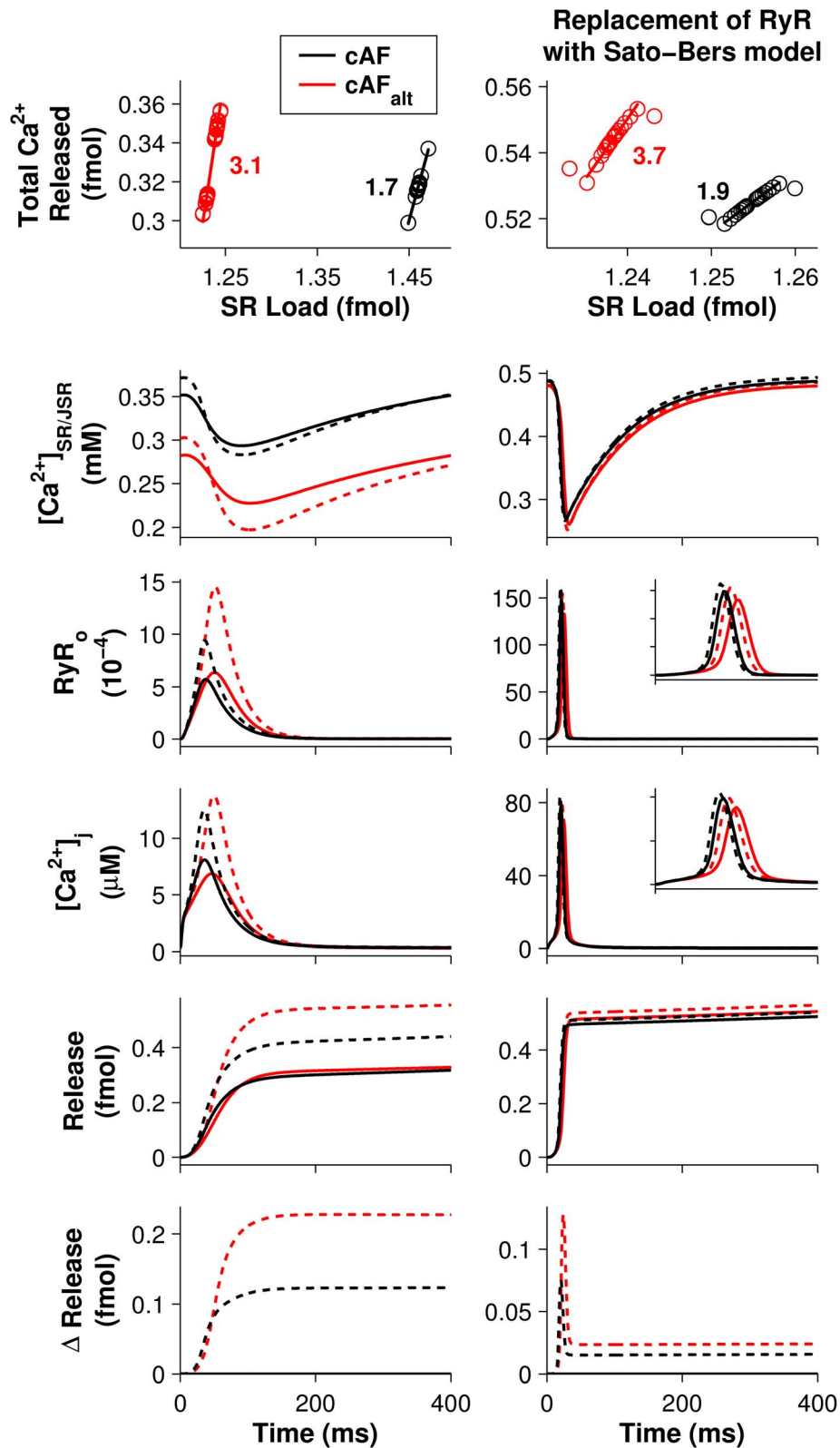


Fig. 7. The effect of RyR inactivation on SR Ca²⁺ release slope. Left column: simulations using the original cAF (black) and cAF_{alt} (red) models. Right column: simulations in which the original RyR model, which included Ca²⁺-dependent inactivation, was replaced with the Sato-Bers RyR model, which utilizes calsequestrin regulation instead (see Table 2). In the Sato-Bers model, the SR is divided into junctional (JSR) and network (NSR) compartments. Top row: Total Ca²⁺ released from the SR is plotted against SR Ca²⁺ load under AP voltage clamp conditions (CL = 400 ms). The line of best fit is also plotted, with its slope value (the SR Ca²⁺ release slope) shown next to the data points. (In column 2, the first beat was excluded.) Modulating RyR inactivation by reducing *k*_{ica} (left column) or *k*₃₄ (right column) by 50% increased the SR Ca²⁺ release slope in both models. Rows 2–6: Traces from a similar set of AP voltage clamp simulations. After reaching steady state (solid lines), SR or NSR load was perturbed at the beginning of

the beat by a large amount (+20 μM , dashed lines) to illustrate the changes affecting SR Ca^{2+} release slope. Row 2: SR (JSR) Ca^{2+} ($[\text{Ca}^{2+}]_{\text{SR/JSR}}$). Row 3: RyR open probability (RyR_o). Row 4: junctional Ca^{2+} ($[\text{Ca}^{2+}]_j$). Row 5: total Ca^{2+} released. Row 6: the difference in total Ca^{2+} release between perturbed and unperturbed (steady state) simulations. Insets in column 2, rows 3–4 show traces from $t=0$ –50 ms. doi:10.1371/journal.pcbi.1004011.g007

Iterated map analysis

Although SR Ca^{2+} release slope is an important component of Ca^{2+} homeostasis, other aspects of Ca^{2+} cycling, such as SR Ca^{2+} uptake, could also have a significant impact. In order to understand how both SR release and uptake contribute to CaT alternans onset at slow pacing rates in human cAF cells, we used an iterated map analysis for investigating Ca^{2+} cycling stability under AP voltage clamp conditions. Three factors affecting Ca^{2+} cycling stability were included in the analysis: SR release, SR uptake, and cellular Ca^{2+} flux across the sarcolemma. The latter factor was included because Ca^{2+} content in the human atrial cell model varied significantly enough to affect alternans threshold predictions.

For each version of the human atrial cell model (cAF and control), we calculated the SR Ca^{2+} release slope (m), the SR Ca^{2+} uptake factor (u), and the cellular Ca^{2+} efflux factor (κ) [28,29] for a range of ki_{Ca} values and pacing rates and compared the value of m to the threshold for alternans. For a typical range of parameter values ($u + \kappa < 1$, see S1 Text), the threshold value of m required for alternans is given by the following equation:

$$m_{\text{thresh}} = \frac{\kappa - 2}{2u + \kappa - 2} + 1 \quad (1)$$

Theoretical analysis predicts that the system is stable when $m < m_{\text{thresh}}$. Eq. 1 is graphed for a range of κ values in Figs. 8A–C (dotted lines). Each curve represents the boundary between stable (no alternans) and unstable (alternans) Ca^{2+} cycling in the u - m plane for a particular value of κ . As κ increases (Fig. 8A–C, dark blue to dark red), the threshold curve steepens, indicating that increased Ca^{2+} extrusion from the cell has a protective effect, helping to restore Ca^{2+} content back to steady state following a perturbation. Thus, a higher value of m is required to reach alternans threshold for higher values of κ . Note that in this theoretical approach, increased Ca^{2+} efflux (κ) has the opposite

effect as in Qu *et al.* [29], suppressing rather than promoting Ca^{2+} alternans.

The effects of changing CL and changing ki_{Ca} are explored for the cAF model in Fig. 8A. At the default ki_{Ca} value (100%), as CL is decreased from 700 ms to 200 ms (–10 ms increments), u decreases, m increases, and the system approaches the alternans threshold given by Eq. 1. The change in κ values is non-monotonic, initially decreasing (orange to green) and then increasing (green to orange) as CL is decreased. However, the change in κ has a minimal effect at small u values, since the threshold curves for different κ values converge at $u=0$. At $\text{CL} < 220$ ms, the cell begins to display alternans in Ca^{2+} cycling, coinciding with the iterated map parameter values residing very close to the theoretically predicted boundary given by Eq. 1 (Fig. 8A, orange X's). When ki_{Ca} is set at 50% of the default cAF value (cAF_{alt} model), a similar trend is observed. However, the 50% ki_{Ca} cAF model reaches threshold at a lower pacing rate ($\text{CL} = 390$ ms for the 50% ki_{Ca} cAF model vs. 210 ms for the 100% ki_{Ca} cAF model, Fig. 8A, X's). This is primarily due to m increasing as ki_{Ca} is decreased, illustrated by the trajectory of the system in the u - m plane as CL is held constant at 390 ms but ki_{Ca} is decreased from 100% to 50% (Fig. 8A).

We next performed the same iterated map analysis for the control atrial cell model with varying CL and ki_{Ca} values (Fig. 8B). When ki_{Ca} is at 100%, u decreases as CL is decreased. However, unlike in the cAF model, in the control case the value of m undergoes a net decrease as CL shortens from 700 to 200 ms. Ultimately, since both m and u decrease as CL is shortened, the control atrial cell (with ki_{Ca} at 100%) fails to reach threshold and remains in the stable, no alternans region. This suggests that alternans in control patients, which occur at $\text{CL} < 250$ ms [8], are driven by voltage rather than Ca^{2+} . As in the cAF model, the alternans threshold CL in the control model can be adjusted by modulating the value of ki_{Ca} (Fig. 8B, $\text{CL} = 390$ ms). However, in the control model, ki_{Ca} must be decreased much more than in the

Table 2. RyR and SR parameters.

Parameters	Original cAF value [19]	Value used in replacement of RyR with Sato-Bers model [27]	Description
ko_{Ca}	30 $\text{mM}^{-2} \text{ms}^{-1}$	N/A	RyR opening rate
K_u	N/A	15 ms^{-1}	CSQN-unbound RyR opening rate
K_b	N/A	0.015 ms^{-1}	CSQN-bound RyR opening rate
τ_b	N/A	0.164 ms	CSQN binding time constant
τ_u	N/A	312 ms	CSQN unbinding time constant
τ_{tr}	N/A	5 ms	JSR refilling time constant
$V_{\text{SR}}/V_{\text{cell}}$	0.035	N/A	SR fractional volume
$V_{\text{JSR}}/V_{\text{cell}}$	N/A	0.0035	JSR fractional volume
$V_{\text{NSR}}/V_{\text{cell}}$	N/A	0.0315	NSR fractional volume
V_{maxSRCaP}	$5.31 \times 10^{-3} \text{ mM/ms}$	$5.04 \times 10^{-2} \text{ mM/ms}$	V_{max} of SERCA pump
k_s	25 ms^{-1}	134 ms^{-1}	SR Ca^{2+} release rate constant
$B_{\text{max_csqn}}$	2.6 mM	0.4 mM	CSQN concentration
K_C	0.65 mM	0.6 mM	Ca^{2+} /CSQN dissociation constant

doi:10.1371/journal.pcbi.1004011.t002

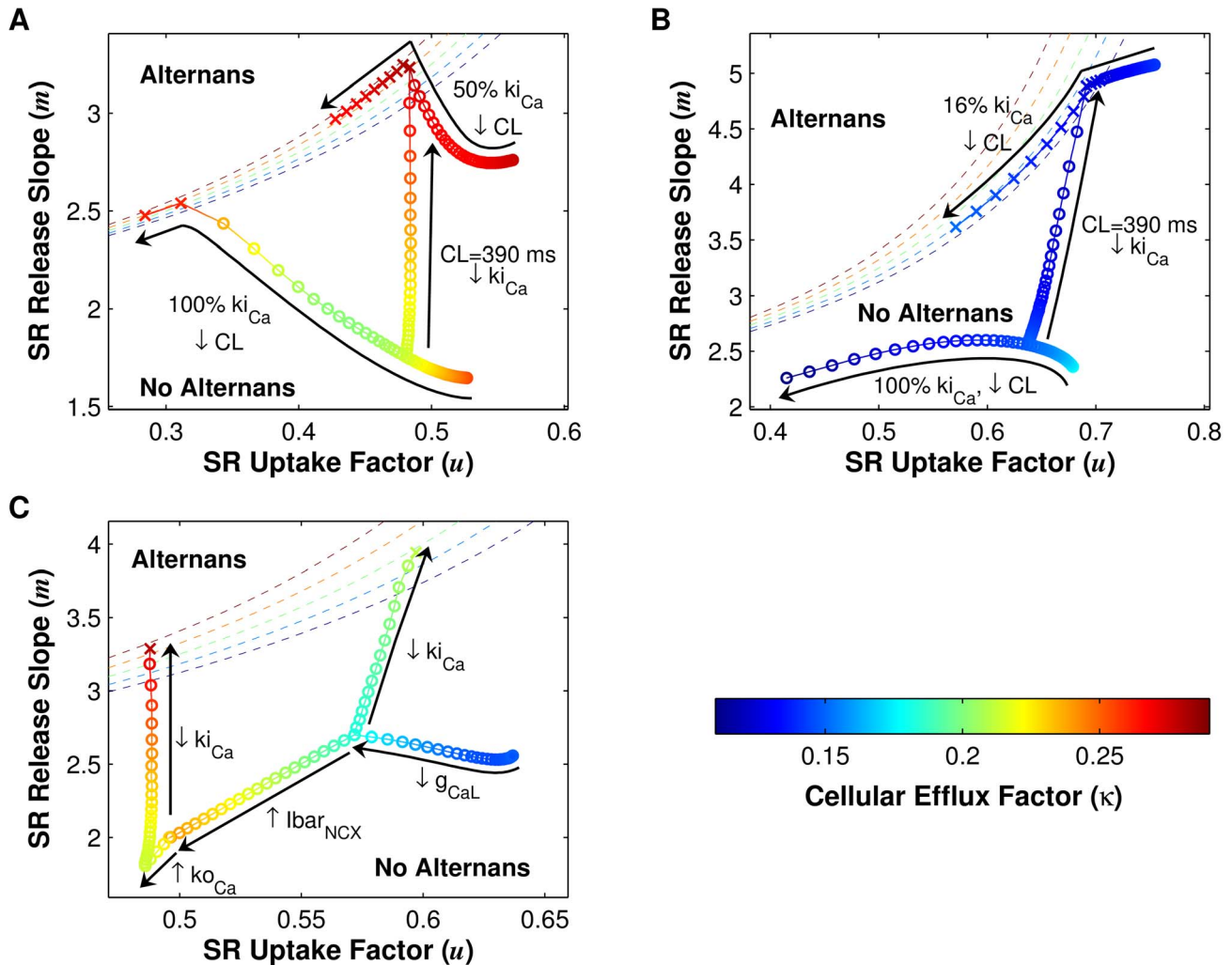


Fig. 8. Iterated map analysis of Ca^{2+} cycling in cAF and control cells. For each panel, SR Ca^{2+} release slope (m) is plotted against SR Ca^{2+} uptake factor (u), with cellular Ca^{2+} efflux factor (κ) values indicated in the color bar. The boundaries between stable (no alternans) and unstable (alternans) regions in the u - m plane are denoted by dashed lines for different values of κ (see Eq. 1). Circles and X's indicate the absence and presence of alternans, respectively. (A) Results for the cAF model. CL is varied, from 700 ms to 200 ms for the 100% ki_{Ca} model and from 700 ms to 300 ms for the 50% ki_{Ca} model (i.e., the cAF_{alt} model), in 10-ms increments. At a CL of 390 ms, ki_{Ca} is scaled from 100% to 50% in 2% increments. (B) Same as in panel A, except that the control cell model is used, and ki_{Ca} is scaled from 100% to 16%. (C) Starting with the control cell parameter values, L-type Ca^{2+} current conductance (g_{CaL}), maximal Na^+/Ca^{2+} exchanger current ($Ibar_{NCX}$), and RyR activation rate constant (ko_{Ca}) are sequentially scaled to cAF values, resulting in net decreases in m and u . Finally, ki_{Ca} is scaled to 50% (as in the cAF_{alt} model), and m increases sufficiently to reach the alternans boundary (red X). If only g_{CaL} is decreased to the cAF value, then alternans threshold is achieved at a higher ki_{Ca} value (72%, green X). doi:10.1371/journal.pcbi.1004011.g008

cAF model in order to reach m_{thresh} at a CL of 390 ms (ki_{Ca} reduced to 16% vs. 50%). The need for dramatic and possibly unrealistic reductions in ki_{Ca} to produce alternans at slow rates in control is consistent with the absence of alternans observed in control patients at $CL \geq 250$ ms [8].

To explain the difference in Ca^{2+} cycling properties of the cAF and control models, we examined the effects of cAF cellular remodeling on iterated map parameters. Stochastic ionic model parameter variation and regression analysis [30] (see S1 Text) predicted that of the ten model parameters altered in the control model to construct the cAF model, seven would have significant effects on alternans threshold CL (these are g_{CaL} , g_{Kur} , ko_{Ca} , $Ibar_{NCX}$, g_{io} , g_{K1} , and g_{Na} , see S8 Figure). Of these seven parameters, three are involved in Ca^{2+} handling (g_{CaL} , ko_{Ca} , and $Ibar_{NCX}$). The effects of changing these three parameters from control to cAF values is depicted sequentially in Fig. 8C: starting

with the default values for the control cell at a CL of 390 ms, first g_{CaL} is decreased and then $Ibar_{NCX}$ and ko_{Ca} are increased to cAF values, resulting in an overall decrease in u and m . Finally, when ki_{Ca} is decreased to the cAF_{alt} value (50%), the large increase in m causes the system to reach m_{thresh} and alternate (Fig. 8C, red X). This illustrates why the control cell is less susceptible to CaT alternans than the cAF cell: at a given ki_{Ca} value and pacing rate, SR uptake efficiency (u) is higher in the control model, thus requiring a large increase in the pacing rate (which decreases u) and/or a large decrease in ki_{Ca} (which increases m) in order to reach m_{thresh} . Of the three cAF parameters which decrease u , however, g_{CaL} is the most important for alternans onset, since remodeling of $Ibar_{NCX}$ and ko_{Ca} decreases m , while remodeling of g_{CaL} increases m . When g_{CaL} is remodeled and $Ibar_{NCX}$ and ko_{Ca} remain at control values, only a 28% decrease in ki_{Ca} is required to reach m_{thresh} (Fig. 8C, green X).

Discussion

Findings and significance

The first goal of this study was to identify the electrophysiological changes in human atrial cells that are responsible for the occurrence of APD alternans at heart rates near rest, as observed in AF patients. Using parameter sensitivity analysis, we found that of the 20 electrophysiological model variables tested, only changes in the RyR inactivation rate constant (k_{iCa}) could produce APD alternans at relatively slow pacing rates in a tissue model of persistent/chronic AF. In particular, decreasing k_{iCa} by 50% (the cAF_{alt} model) produced a good match to clinical data. We next aimed to provide mechanistic insight into why disruption of RyR kinetics, together with other electrophysiological changes occurring in AF, leads to alternans onset at pacing rates near rest. We established that alternans in the cAF_{alt} model at the onset CL were Ca²⁺-driven rather than voltage-driven, and that they depended upon SR Ca²⁺ release. Furthermore, CaT alternans occurred in the cAF_{alt} model at relatively long CLs because of steep SR Ca²⁺ release slope and decreased SR Ca²⁺ uptake efficiency. Lastly, we demonstrated that the ability to generate alternans at slower pacing rates by modulating k_{iCa} depended upon the negative feedback properties of SR Ca²⁺ release.

This study is the first to identify a possible mechanism for alternans occurring at slow heart rates in AF patients. Our novel findings show that alternans at slow rates is Ca²⁺-driven, brought about by AF-associated remodeling of the Ca²⁺ handling system in atrial cells. Clinical and experimental research has shown that atrial alternans is associated with disease progression in AF patients [8] and with increased AF susceptibility after myocardial infarction [31,32] and atrial tachycardia [33,34] in animal models. Additionally, CaT alternans have been studied in animal atrial myocytes [17,18,35] and in the intact atria of AF-prone mice [36]. However, the precise cellular mechanism underlying alternans at heart rates near rest in the remodeled human atria has not been previously identified, and a direct relationship between human AF and CaT alternans in the atria has not been established until now. Elucidating the mechanism driving alternans at slow rates is particularly important because APD oscillations appear to be closely linked to AF initiation [8]. If APD alternans play a direct role in AF initiation, the onset of alternans at slower pacing rates would indicate an increased susceptibility to arrhythmia in AF patients, consistent with clinical observations [8]. Identification of this mechanism would thus provide a significant scientific and clinical benefit, improving our understanding of arrhythmogenesis and aiding in the development of new targeted therapies for AF.

In this study, we demonstrate how different aspects of AF remodeling contribute to Ca²⁺-driven alternans onset at slower heart rates using a theoretical analysis of Ca²⁺ cycling. This analysis allowed us to quantitatively assess CaT alternans threshold under AP voltage clamp conditions in a detailed electrophysiological model, providing valuable insights into the effects of AF electrophysiological remodeling on Ca²⁺ handling and alternans. Furthermore, we identify a critical aspect of SR Ca²⁺ release—inactivation of the RyR—which is necessary for CaT alternans to occur at slow heart rates. These findings extend mechanistic insight about proarrhythmic ventricular Ca²⁺ remodeling [15,37,38] to the atria and may inform new therapeutic strategies to target the RyR and suppress Ca²⁺-driven alternans in the atria for the purposes of preventing or treating AF [36,39].

RyR dysregulation in AF

The RyR has been the focus of several studies concerning trigger-mediated AF. In particular, disruption of RyR regulation

has been shown to promote AF through increased RyR open probability, diastolic SR Ca²⁺ leak, and delayed afterdepolarizations [12,39,40]. Here we identify an additional pathological consequence of the disruption of RyR regulation in AF: Ca²⁺-driven alternans. Similar to what has been demonstrated with regards to Ca²⁺ sparks and triggered activity [39], we found that CaT alternans is coupled to voltage primarily through upregulated I_{NCX}, thus driving the generation of APD alternans. The RyR's central role in both alternans and triggers has important clinical implications, given the proarrhythmic consequences of interaction between ectopic activity and the arrhythmogenic substrate created by voltage alternans [41]. New drug treatments to restore the normal function of the RyR and NCX, and thereby prevent arrhythmogenic triggers and alternans, have the potential to provide more effective alternatives to current AF drug therapies which target voltage-gated ion channels and often have proarrhythmic side effects [39].

The signaling pathways involved in RyR dysfunction in AF have been the focus of much active research over the past several years [39,40]. Possible molecular mechanisms which could account for reduced RyR inactivation include RyR hyperphosphorylation by CAMKII and PKA and dissociation of the RyR subunit FKBP12.6, which have been shown to increase RyR open probability and promote arrhythmia [42], although the exact role of these mechanisms in RyR dysregulation are still debated [43]. Calmodulin has also been shown to interact directly with the RyR to decrease its open probability [44]. Metabolic factors may play a role, since modulation of the RyR as a result of glycolytic inhibition has been linked to atrial alternans in non-AF animal models [16,17,35]. Such metabolic impairment is thought to contribute to profibrillatory remodeling in the atria [45–47]. The cAF_{alt} model, with its reduction in k_{iCa} , can be considered a phenomenological representation of the various signaling pathway disruptions leading to alternans, which were not represented in the original cAF model. As more information becomes available, incorporation of these signaling mechanisms into computational models may provide additional insights into how reduction in RyR inactivation leads to Ca²⁺-driven alternans at slow heart rates in AF patients.

The role of RyR refractoriness in CaT alternans

There is debate over whether CaT alternans depend primarily on SR Ca²⁺ load alternation or on RyR refractoriness [21,41,48]. Recent experiments [18,49] and simulation studies [50–53] have shown that RyR refractoriness can drive CaT alternans under conditions where near-identical SR loads produce different amounts of SR release. In some simulation studies, this phenomenon was restricted to limited parameter values, clamping conditions, and cycle lengths [51,52], while in a more recent modeling study focusing on atrial cells, SR load-independent alternans occurred over a broad range of pacing rates when the number of t-tubules was reduced [53]. Of note is the fact that many of these studies [51–53] utilized the same RyR gating scheme as this current study, yet they identified various mechanisms for CaT alternans. This demonstrates that the relative importance of the various mechanisms, whether SR load-driven, RyR refractoriness-driven, or otherwise, is highly context-dependent.

Although exploring the issue of SR load vs. RyR refractoriness was beyond the goals of the current study, our results suggest that in human cAF, both SR load alternation and RyR refractoriness are involved in alternans genesis at slower pacing rates. In our cAF_{alt} model, alternation in all SR Ca²⁺ release variables, including [Ca²⁺]_{SR}, RyR open probability, and RyR inactivated

probability, was necessary for alternans at the onset CL of 400 ms (Fig. 6). In addition, SR uptake flux (J_{serca}) enhanced alternans when clamped (Fig. 6) and therefore suppressed alternans under normal pacing conditions, suggesting that SR load is indeed an important driver of CaT alternans in cAF and that upregulation of the SERCA pump may be an important therapeutic strategy for diminishing alternans. We also showed that CaT alternans occurred in the cAF_{alt} model at slow pacing rates because decreased RyR inactivation resulted in steepening of the SR release-load relationship. Together, these results indicate that the interplay between SR load and RyR kinetics is responsible for alternans onset in human AF.

Other potential mechanisms for alternans susceptibility

The mechanisms for human atrial alternans susceptibility are likely to encompass a range of complex interactions at multiple scales of biology, which extend beyond the cellular-level mechanisms found here. In this study we examined the behavior of an atrial cell with well-developed t-tubules [19]. Research has shown that rat atrial cells have variable levels of t-tubule organization [54]. Such variation, if present in human atrial cells, would result in subcellular Ca^{2+} gradients which could make cells more susceptible to alternans [17,55,56]. Models of atrial myocytes incorporating detailed spatial descriptions [57] and local control of Ca^{2+} [58] will aid in future investigations of the subcellular mechanisms of cAF-related alternans.

In addition, the complex structure of the atria, including its normal conduction pathways [59] and fibrotic remodeling in AF [60,61], may promote heterogeneity and discordant alternans, which significantly affect alternans dynamics and reentry initiation [9,62]. Consideration of these factors in the future will further enrich the mechanistic insight gained from this current study and will advance our understanding of the role that alternans play in AF arrhythmogenesis.

Limitations

In many cell models, the effective refractory period (ERP) is not consistent with ERP at the tissue level [63]. Electrotonic effects in tissue and the whole heart can shorten or lengthen APD depending on which structures and cell types are coupled to each other. Furthermore, alternans in single cell models may not be predictive of alternans in tissue, where conduction alternans can occur. This was the case for the control atrial tissue model, in which loss of capture occurred at a CL of 260 ms before reaching the very fast pacing rates at which APD alternans were observed in human control patients (CL = 218 ± 30 ms) [8]. However, alternans onset at clinically observed rates occurred in the single-cell control model (200 ms CL, S9 Figure, black curve) and when k_{Ca} was reduced by 5% (230 ms CL, S9 Figure, red curve). This suggests that the ionic model may not be well-constrained for tissue simulations at very fast rates. However, this issue did not affect the study of alternans onset at slower pacing rates, as was observed in AF patients.

Our ionic model variable clamping protocol, which involved separately clamping the even or odd beat waveforms, was used to test for model variables which could robustly suppress alternans when clamped to either of two very different waveforms. An alternative approach would be to clamp model variables to the single unstable, non-alternating waveform obtained using a control algorithm [64]. This approach would allow more precise assessment of fixed point stability, since clamping is done at the point of instability rather than during the bistable (alternans) endpoint. However, for the purposes of quantifying the most important variables influencing instability, the clamping protocol

used in this study was sufficient to identify the central role of SR Ca^{2+} release, which was later confirmed through iterated map analysis.

Recent experimental evidence points towards local SR Ca^{2+} depletion, rather than Ca^{2+} -dependent RyR inactivation, as the main mechanism of SR release termination [23–26]. Although alternans in the cAF_{alt} model relied on Ca^{2+} -dependent RyR inactivation, other termination mechanisms which rely on SR Ca^{2+} (used in the Sato-Bers RyR model) may have similar effects on SR release slope and alternans susceptibility (Fig. 7, column 2). However, with the Sato-Bers RyR model, alternans and other complex oscillations began at the baseline pacing rate (750 ms CL, S10 Figure) and did not display the same rate dependence observed in patients [8]. In addition, large oscillations in CaT amplitude did not couple as strongly to voltage as with the original RyR, and oscillations were also attenuated in tissue (S10 Figure). Further work is needed to develop atrial cell models which incorporate current mechanistic understanding of SR Ca^{2+} release and which can also reproduce AF-related alternans rate dependence in tissue.

Conclusion

AF is associated with progressive changes in alternans onset in the human atria, with alternans occurring at slower heart rates as AF severity worsens. We found that the differences in alternans onset between AF and control patients could be accounted for by changes in the inactivation rate of the RyR in a model of human atrial cAF-remodeled tissue. Single-cell simulations revealed that alternans at these slow heart rates were driven by abnormal Ca^{2+} handling and the development of CaT alternans, and that changes in CaT alternans threshold resulted from steepening of the SR Ca^{2+} release slope, decreased SR Ca^{2+} uptake efficiency, and decreased inactivation of the RyR. These findings provide important insight into the mechanisms underlying proarrhythmic APD alternans occurring at slow heart rates in cAF patients. Such insight may aid in the development of targeted therapies and new treatment strategies for AF in the future.

Methods

Human AF tissue model

In order to investigate ionic mechanisms in human AF that contribute to the generation of atrial alternans at the tissue level, we created a computer model of human atrial tissue incorporating ionic remodeling associated with cAF. The atrial tissue preparation had dimensions of $0.33 \times 0.33 \times 9.9$ mm³ (Fig. 1A), similar to the one used by Krummen *et al.* [65] Human atrial cell membrane kinetics were represented by a modified version of the Grandi-Pandit-Voigt (GPV) human atrial action potential model [19], which we refer to as the GPV_m model. Detailed explanation and justification of the GPV_m model modifications are provided in the supplement (S1, S2 Texts). Different types of human atrial tissue were modeled individually as homogenous tissue preparations, with each incorporating ionic changes appropriate for each tissue type. Both control and cAF-remodeled tissue, as well as left and right atrial tissue, were modeled using the parameter changes specified by Grandi *et al.* [19] (see S1 Text). The isotropic bulk conductivity value for the tissue was tuned to produce a conduction velocity of 0.62 m/s in control tissue [59,66]. When cAF ionic remodeling was incorporated, the same bulk conductivity value produced a conduction velocity of 0.59 m/s. These values are within the reported ranges for control and AF conduction velocities [67].

Protocols for evaluating alternans in the human AF tissue model

We assessed alternans in the human AF tissue model by applying the clinical pacing protocol used by Narayan *et al.* to induce alternans in AF patients [8]. The tissue model was first initialized at all nodes with steady-state values from a single cell paced at 750-ms CL. The tissue was then paced from the stimulus electrode (Fig. 1A) for 20 beats at 750-ms CL and then for 74 beats at each subsequent CL, starting from 500 ms and shortened in 50-ms steps to 300 ms, and then shortened in 10-ms steps, until loss of capture or conduction block occurred.

Voltage traces from the recording electrode (Fig. 1A) were analyzed for APD alternans. APD was calculated as the time from maximal upstroke velocity to 90% repolarization of V_m from phase II amplitude. Alternans magnitude was quantified as the mean magnitude of change in APD over the last 10 pairs of beats (11 beats total). APD alternans normalized magnitude (ANM), obtained by dividing the alternans magnitude by the mean APD over the last 10 beats, was used to compare alternans between cells of varying APD. Alternans onset CL was defined as the longest CL for which ANM was greater than 5% [8].

Sensitivity of alternans to ionic model parameters

To identify cellular changes which could account for the onset of alternans in AF patients at CLs of 300–500 ms [8], we explored how ANM varied in human AF tissue models of both the left and right atrium as a result of changes in ionic model parameters. Of the 20 ionic model parameters tested, 10 were parameters altered in the GPV model to represent cAF [19]; others were associated with L-type Ca^{2+} current (I_{CaL}), rapidly activating potassium current (I_{Kr}), SR uptake, or SR release (Table 1). We scaled parameter values one at a time to 25–200% of the default left or right atrium values specified by Grandi *et al.* [19]; for each parameter value within this range, simulations were conducted to determine the presence of alternans (282 simulations total). In AF patients, average alternans onset CL was >300 ms [8], so pacing and alternans analysis was restricted to CLs ≥ 300 ms.

Clamping protocols

After identifying conditions under which APD alternans magnitude and onset CL matched clinical observations, we utilized two different clamping approaches in order to investigate the key cellular properties that gave rise to these alternans, as described below. Further explanation of the rationale behind these methods can be found in Results.

Ionic model variable clamps. To determine which human atrial ionic model variables drive the occurrence of alternans, we clamped individual ion currents and state variables in a single-cell model paced at a CL exhibiting alternans [15]. A model variable was clamped to its steady-state even or odd beat trace for the duration of 50 beats. This procedure was repeated for different model variables (membrane currents, SR fluxes, and all state variables excluding buffer concentrations), and APD alternans magnitude was quantified at the end of the 50 clamped beats. Additionally, the magnitude of alternans in $\Delta[\text{Ca}^{2+}]_i$ was quantified in the same manner as APD alternans magnitude, with $\Delta[\text{Ca}^{2+}]_i$ calculated as the difference between peak $[\text{Ca}^{2+}]_i$ during the beat and minimum $[\text{Ca}^{2+}]_i$ during the preceding diastolic interval (DI). Model variables were considered critical for alternans if clamping them to either the even or odd beat reduced both APD and CaT alternans magnitudes by $>99\%$ of baseline [15].

AP clamp. To evaluate the Ca^{2+} cycling properties of the human atrial cell model under different pacing rates and parameter values, the following equation was used to clamp V_m to a generic atrial AP-like waveform so that comparisons between different conditions would not be influenced by variations in V_m :

$$V_m = \begin{cases} V_{\text{max}} + \frac{t}{\text{APD}} \cdot (V_{\text{rest}} - V_{\text{max}}) & n \cdot \text{CL} \leq t < n \cdot \text{CL} + \text{APD} \\ V_{\text{rest}} & n \cdot \text{CL} + \text{APD} \leq t < (n+1) \cdot \text{CL} \end{cases}$$

This approach has been used previously to investigate Ca^{2+} cycling properties in ventricular myocyte models [22,50]. We set $V_{\text{max}} = 10$ mV, $V_{\text{rest}} = -75$ mV, and APD = 200 ms. CL ranged from 200 to 700 ms.

The AP clamp enabled evaluation of Ca^{2+} cycling stability in the human atrial cell model via an iterated map analysis [22,28,68]. We used a similar approach as Qu *et al.* [29], where SR load and total Ca^{2+} content of the cell are tracked from beat to beat. In our analysis, Ca^{2+} cycling stability depended upon three iterated map parameters: SR Ca^{2+} release slope (m), SR Ca^{2+} uptake factor (u), and cellular Ca^{2+} efflux factor (κ). A detailed derivation of the iterated map stability criteria can be found in S1 Text.

To compute the iterated map parameters, a single atrial cell was repeatedly clamped to the AP waveform until model variables reached steady state. Following this, $[\text{Ca}^{2+}]_{\text{SR}}$ was perturbed by $\pm 1\%$ at the beginning of an even beat, and total SR load, release, uptake, and cellular Ca^{2+} efflux per beat were recorded for the following 10 beats. For the Sato-Bers model, the first beat was excluded since it deviated noticeably from the linear response of later beats. This procedure was repeated starting with an odd beat so that data from a total of 40 beats were recorded (36 beats for the Sato-Bers model). Lastly, m , u , and κ were computed as the slopes of the linear least-squares fit of the data (see S1 Text).

Numerical methods

The monodomain and ionic model equations were solved using the Cardiac Arrhythmia Research Package (CARP; Cardiosolv, LLC) [69]. Details on the numerical techniques used by CARP have been described previously [70,71]. A time step of 20 μs was used for all simulations.

Supporting Information

S1 Figure Comparison of original and modified versions of the GPV ionic model in tissue. At 400-ms CL, the original GPV model did not propagate robustly in tissue (black line). When the fast sodium current kinetics was replaced with the kinetics from the Luo-Rudy dynamic model (LRd), normal propagation occurred (blue line). Applying the fast equilibrium approximation to select buffers (see S2 Text) had a negligible effect on simulation results (dotted green line). (TIF)

S2 Figure Sensitivity of APD alternans magnitude to ionic model parameters in RA cAF tissue during pacing. Parameter sensitivity analysis was performed in tissue with the right atrium version of the GPV model incorporating cAF remodeling, in order to identify ionic model parameters that influence alternans. APD alternans normalized magnitude (ANM) is indicated by the colorbar (≥ 0.05 considered significant). Parameters were scaled one at a time between 25% (short ticks) and 200% (long ticks) of their AF model values (25% increments). Results were similar to those obtained with the left atrium version of the model (see Fig. 2A), with alternans occurring at the longest

CLs only when the RyR inactivation rate constant (k_{iCa}) was decreased.

(TIF)

S3 Figure APD alternans magnitudes in cAF_{alt} tissue.

The tissue preparation was paced from the stimulus electrode (see Fig. 1A), and APD alternans normalized magnitudes (ANMs) were quantified at each cycle length for every node along the tissue. When significant alternans was present in the tissue ($ANM > 0.05$), all nodes had concordant alternans of similar magnitude.

(TIF)

S4 Figure Voltage and Ca²⁺ odd beat clamps for the single-cell cAF_{alt} model.

Traces of transmembrane potential (V_m , row 1), intracellular Ca²⁺ ($[Ca^{2+}]_i$, row 2), and SR Ca²⁺ ($[Ca^{2+}]_{SR}$, row 3) from two consecutive beats are superimposed to show alternans between even (red) and odd (blue) beats. Column 1: the unclamped cAF_{alt} cell paced to steady state at 400-ms CL displayed alternans in V_m and Ca²⁺. The blue traces depicted in column 1 were used to clamp V_m (column 2), $[Ca^{2+}]_i$ (column 3), or $[Ca^{2+}]_{SR}$ (column 4). Alternans persisted when V_m or $[Ca^{2+}]_i$ was clamped, but clamping $[Ca^{2+}]_{SR}$ eliminated alternans.

(TIF)

S5 Figure SR Ca²⁺ release parameter even beat clamps for the single-cell cAF_{alt} model.

Traces of transmembrane potential (V_m , row 1), intracellular Ca²⁺ ($[Ca^{2+}]_i$, row 2), and SR Ca²⁺ ($[Ca^{2+}]_{SR}$, row 3) from two consecutive beats are superimposed to show alternans between even (red) and odd (blue) beats. Traces from the even beat at 400-ms CL pacing were used to clamp the relevant variable and are shown in row 4. Clamping RyR inactivated probability (RyR_i , column 1), RyR open probability (RyR_o , column 2), junctional Ca²⁺ ($[Ca^{2+}]_j$, column 3), or SR Ca²⁺ release flux ($J_{SR\text{Carel}}$, column 4) eliminated alternans in V_m and Ca²⁺.

(TIF)

S6 Figure SR Ca²⁺ release parameter odd beat clamps for the single-cell cAF_{alt} model.

Traces of transmembrane potential (V_m , row 1), intracellular Ca²⁺ ($[Ca^{2+}]_i$, row 2), and SR Ca²⁺ ($[Ca^{2+}]_{SR}$, row 3) from two consecutive beats are superimposed to show alternans between even (red) and odd (blue) beats. Traces from the odd beat at 400-ms CL pacing were used to clamp the relevant variable and are shown in row 4. Clamping RyR inactivated probability (RyR_i , column 1), RyR open probability (RyR_o , column 2), junctional Ca²⁺ ($[Ca^{2+}]_j$, column 3), or SR Ca²⁺ release flux ($J_{SR\text{Carel}}$, column 4) eliminated alternans in V_m and Ca²⁺.

(TIF)

S7 Figure Sub-sarcolemmal parameter clamps for the single-cell cAF_{alt} model.

Traces of transmembrane potential (V_m , row 1), intracellular Ca²⁺ ($[Ca^{2+}]_i$, row 2), and SR Ca²⁺ ($[Ca^{2+}]_{SR}$, row 3) from two consecutive beats are superimposed to show alternans between even (red) and odd (blue) beats. Traces from the even or odd beat at 400-ms CL pacing were used to clamp the relevant variable and are shown in row 4. Clamping sub-sarcolemmal Ca²⁺ ($[Ca^{2+}]_{sl}$) to the even beat (column 1) eliminated alternans in V_m and Ca²⁺, but clamping $[Ca^{2+}]_{sl}$ to the odd beat (column 2) produced small alternans in V_m and $[Ca^{2+}]_i$ and large alternans in $[Ca^{2+}]_{SR}$. Clamping sub-sarcolemmal Na⁺/Ca²⁺ exchanger current (I_{NCXsl}) to the even beat (column 3) eliminated alternans in APD but produced large alternans in

$[Ca^{2+}]_i$ and $[Ca^{2+}]_{SR}$. Clamping I_{NCXsl} to the odd beat (column 4) eliminated alternans in V_m and Ca²⁺.

(TIF)

S8 Figure Multivariable regression between ionic model parameters and alternans threshold CL.

(A) Bar graph of regression coefficient magnitudes. Twenty ionic model parameters were varied stochastically over 500 simulations to assess their effects on alternans cycle length (CL). Of the 500 simulations, 83 were excluded from the analysis because alternans threshold CL was below 100 ms or above 750 ms. Linear regression coefficients for each of the parameters are plotted in order of decreasing magnitude, with positive values plotted in red and negative values plotted in blue. Asterisks indicate $p < 0.05$ for the t -statistic. (B) Bar graph of the predicted contribution of parameters to alternans threshold CL in the cAF-remodeled cell. Ten of the twenty parameters used in the regression analysis were altered from control values to represent cAF remodeling (increases and decreases indicated by upward and downward arrows, respectively). Parameters whose changes were predicted to increase (decrease) the alternans CL are plotted in red (blue). Some unaltered parameters had nonzero predicted contributions to alternans threshold CL due to nonzero sample means from the regression analysis. The alternans threshold CL predicted by regression analysis (245 ms) was very close to the actual alternans threshold CL determined by simulation (244 ms).

(TIF)

S9 Figure Single-cell APD restitution in control model.

With default model parameter values, APD alternans occurred at 200 ms CL (black). When the RyR inactivation rate constant (k_{iCa}) was reduced to 95%, alternans occurred at slightly longer CLs (red). These results were comparable to alternans onset data from control patients [8].

(TIF)

S10 Figure APD and CaT oscillations in single-cell and tissue models with Sato-Bers RyR formulation.

Control (black), cAF (red), and cAF_{alt} (dotted red line) versions of the model using the Sato-Bers RyR [27] were implemented in single cell (A and B) and in tissue (C and D). In the cAF_{alt} model, the calsequestrin-bound RyR closing rate (k_{34}) was decreased by 50%. APD (A and C) and CaT (B and D) restitution data are plotted showing the mean \pm SD range (control, gray shading, not visible; cAF, pink shading; cAF_{alt}, red hatching). Oscillations in APD and CaT included but were not limited to alternans. Oscillations exhibited the reverse of the rate dependence observed in models using the original RyR formulation, with larger oscillations at longer CL. APD oscillations in these models were diminished as compared to the original models (see Fig. 1), and both APD and CaT oscillations were attenuated in tissue.

(TIF)

S1 Text Supplemental methods.

(PDF)

S2 Text Supplemental equations.

(PDF)

Author Contributions

Conceived and designed the experiments: KCC JDB NAT. Performed the experiments: KCC. Analyzed the data: KCC. Contributed reagents/materials/analysis tools: KCC JDB. Wrote the paper: KCC NAT.

References

- Feinberg WM, Blackshear JL, Laupacis A, Kronmal R, Hart RG (1995) Prevalence, Age Distribution, and Gender of Patients With Atrial Fibrillation. Analysis and Implications. *Arch Intern Med* 155: 469–473.
- Go AS, Hylek EM, Phillips KA, Chang Y, Henault LE, et al. (2001) Prevalence of Diagnosed Atrial Fibrillation in Adults: National Implications for Rhythm Management and Stroke Prevention: the AnTicoagulation and Risk Factors In Atrial Fibrillation (ATRIA) Study. *JAMA* 285: 2370–2375.
- Coyne KS, Paramore C, Grandy S, Mercader M, Reynolds M, et al. (2006) Assessing the direct costs of treating nonvalvular atrial fibrillation in the United States. *Value Health* 9: 348–356.
- Nattel S (2002) New ideas about atrial fibrillation 50 years on. *Nature* 415: 219–226.
- Nattel S, Burstein B, Dobrev D (2008) Atrial remodeling and atrial fibrillation: mechanisms and implications. *Circ Arrhythmia Electrophysiol* 1: 62–73.
- Kim B-S, Kim Y-H, Hwang G-S, Pak H-N, Lee SC, et al. (2002) Action potential duration restitution kinetics in human atrial fibrillation. *J Am Coll Cardiol* 39: 1329–1336.
- Narayan SM, Bode F, Karasik PL, Franz MR (2002) Alternans of Atrial Action Potentials During Atrial Flutter as a Precursor to Atrial Fibrillation. *Circulation* 106: 1968–1973.
- Narayan SM, Franz MR, Clopton P, Pruvot EJ, Krummen DE (2011) Repolarization alternans reveals vulnerability to human atrial fibrillation. *Circulation* 123: 2922–2930.
- Franz MR, Jamal SM, Narayan SM (2012) The role of action potential alternans in the initiation of atrial fibrillation in humans: a review and future directions. *Europace* 14: v58–64.
- Hiroamoto K, Shimizu H, Furukawa Y, Kanemori T, Mine T, et al. (2005) Discordant repolarization alternans-induced atrial fibrillation is suppressed by verapamil. *Circ J* 69: 1368–1373.
- Lalani GG, Schrickler AA, Clopton P, Krummen DE, Narayan SM (2013) Frequency analysis of atrial action potential alternans: a sensitive clinical index of individual propensity to atrial fibrillation. *Circ Arrhythmia Electrophysiol* 6: 859–867.
- Nattel S, Dobrev D (2012) The multidimensional role of calcium in atrial fibrillation pathophysiology: mechanistic insights and therapeutic opportunities. *Eur Heart J* 33: 1870–1877.
- Heijman J, Voigt N, Nattel S, Dobrev D (2012) Calcium handling and atrial fibrillation. *Wiener medizinische Wochenschrift* 162: 287–291.
- Narayan SM, Bayer JD, Lalani G, Trayanova NA (2008) Action potential dynamics explain arrhythmic vulnerability in human heart failure: a clinical and modeling study implicating abnormal calcium handling. *J Am Coll Cardiol* 52: 1782–1792.
- Bayer JD, Narayan SM, Lalani GG, Trayanova NA (2010) Rate-dependent action potential alternans in human heart failure implicates abnormal intracellular calcium handling. *Heart Rhythm* 7: 1093–1101.
- Hüser J, Wang YG, Sheehan KA, Cifuentes F, Lipsius SL, et al. (2000) Functional coupling between glycolysis and excitation-contraction coupling underlies alternans in cat heart cells. *J Physiol* 524: 795–806.
- Blatter LA, Kockskämper J, Sheehan KA, Zima A V, Huser J, et al. (2002) Local calcium gradients during excitation-contraction coupling and alternans in atrial myocytes. *J Physiol* 546: 19–31.
- Shkryl VM, Maxwell JT, Domeier TL, Blatter LA (2012) Refractoriness of sarcoplasmic reticulum Ca²⁺ release determines Ca²⁺ alternans in atrial myocytes. *Am J Physiol Heart Circ Physiol* 302: H2310–20.
- Grandi E, Pandit S V, Voigt N, Workman AJ, Dobrev D, et al. (2011) Human Atrial Action Potential and Ca²⁺ Model: Sinus Rhythm and Chronic Atrial Fibrillation. *Circ Res* 109: 1055–1066.
- Wan X, Cutler M, Song Z, Karma A, Matsuda T, et al. (2012) New experimental evidence for mechanism of arrhythmogenic membrane potential alternans based on balance of electrogenic I(NCX)/I(Ca) currents. *Heart Rhythm* 9: 1698–1705.
- Diaz ME, O'Neill SC, Eisner DA (2004) Sarcoplasmic reticulum calcium content fluctuation is the key to cardiac alternans. *Circ Res* 94: 650–656.
- Xie L-H, Sato D, Garfinkel A, Qu Z, Weiss JN (2008) Intracellular Ca alternans: coordinated regulation by sarcoplasmic reticulum release, uptake, and leak. *Biophys J* 95: 3100–3110.
- Sobie EA, Lederer WJ (2012) Dynamic local changes in sarcoplasmic reticulum calcium: physiological and pathophysiological roles. *J Mol Cell Cardiol* 52: 304–311.
- Radwański PB, Belevych AE, Brunello L, Carnes CA, Györke S (2013) Store-dependent deactivation: cooling the chain-reaction of myocardial calcium signaling. *J Mol Cell Cardiol* 58: 77–83.
- Laver DR, Kong CHT, Imtiaz MS, Cannell MB (2013) Termination of calcium-induced calcium release by induction decay: an emergent property of stochastic channel gating and molecular scale architecture. *J Mol Cell Cardiol* 54: 98–100.
- Stern MD, Ríos E, Maltsev VA (2013) Life and death of a cardiac calcium spark. *J Gen Physiol* 142: 257–274.
- Sato D, Bers DM (2011) How does stochastic ryanodine receptor-mediated Ca leak fail to initiate a Ca spark? *Biophys J* 101: 2370–2379.
- Weiss JN, Karma A, Shiferaw Y, Chen P-S, Garfinkel A, et al. (2006) From pulsus to pulseless: the saga of cardiac alternans. *Circ Res* 98: 1244–1253.
- Qu Z, Shiferaw Y, Weiss J (2007) Nonlinear dynamics of cardiac excitation-contraction coupling: An iterated map study. *Phys Rev E* 75: 011927.
- Sobie EA (2009) Parameter sensitivity analysis in electrophysiological models using multivariable regression. *Biophys J* 96: 1264–1274.
- Miyauchi Y, Zhou S, Okuyama Y, Miyauchi M, Hayashi H, et al. (2003) Altered atrial electrical restitution and heterogeneous sympathetic hyperinnervation in hearts with chronic left ventricular myocardial infarction: implications for atrial fibrillation. *Circulation* 108: 360–366.
- Kettlwell S, Burton FL, Smith GL, Workman AJ (2013) Chronic myocardial infarction promotes atrial action potential alternans, afterdepolarizations, and fibrillation. *Cardiovasc Res* 99: 215–224.
- Jousset F, Tenkorang J, Vesin J-M, Pascale P, Ruchat P, et al. (2012) Kinetics of atrial repolarization alternans in a free-behaving ovine model. *J Cardiovasc Electrophysiol* 23: 1003–1012.
- Monigatti-Tenkorang J, Jousset F, Pascale P, Vesin J-M, Ruchat P, et al. (2014) Intermittent Atrial Tachycardia Promotes Repolarization Alternans and Conduction Slowing During Rapid Rates, and Increases Susceptibility to Atrial Fibrillation in a Free-Behaving Sheep Model. *J Cardiovasc Electrophysiol* 25: 418–427.
- Kockskämper J, Zima A V, Blatter LA (2005) Modulation of sarcoplasmic reticulum Ca²⁺ release by glycolysis in cat atrial myocytes. *J Physiol* 564: 697–714.
- Xie W, Santulli G, Guo X, Gao M, Chen B-X, et al. (2013) Imaging atrial arrhythmic intracellular calcium in intact heart. *J Mol Cell Cardiol* 64: 120–123.
- Livshitz LM, Rudy Y (2007) Regulation of Ca²⁺ and electrical alternans in cardiac myocytes: role of CAMKII and repolarizing currents. *Am J Physiol Heart Circ Physiol* 292: H2854–66.
- Belevych AE, Terentyev D, Viatchenko-Karpinski S, Terentyeva R, Sridhar A, et al. (2009) Redox modification of ryanodine receptors underlies calcium alternans in a canine model of sudden cardiac death. *Cardiovasc Res* 84: 387–395.
- Dobrev D, Voigt N, Wehrens XHT (2011) The ryanodine receptor channel as a molecular motif in atrial fibrillation: pathophysiological and therapeutic implications. *Cardiovasc Res* 89: 734–743.
- Lederer WJ, Bers DM, Eisner DA, Marx SO, Marks AR (2013) Dysfunctional ryanodine receptors in the heart: New insights into complex cardiovascular diseases. *J Mol Cell Cardiol* 58: 225–231.
- Laurita KR, Rosenbaum DS (2008) Cellular mechanisms of arrhythmogenic cardiac alternans. *Prog Biophys Mol Biol* 97: 332–347.
- Dobrev D, Wehrens XHT (2014) Role of RyR2 Phosphorylation in Heart Failure and Arrhythmias: Controversies Around Ryanodine Receptor Phosphorylation in Cardiac Disease. *Circ Res* 114: 1311–1319.
- Houser SR (2014) Role of RyR2 Phosphorylation in Heart Failure and Arrhythmias: Protein Kinase A-Mediated Hyperphosphorylation of the Ryanodine Receptor at Serine 2808 Does Not Alter Cardiac Contractility or Cause Heart Failure and Arrhythmias. *Circ Res* 114: 1320–1327.
- Arnáiz-Cot JJ, Damon BJ, Zhang X-H, Cleemann L, Yamaguchi N, et al. (2013) Cardiac calcium signaling pathologies associated with defective calmodulin regulation of type 2 ryanodine receptor. *J Physiol* 591: 4287–4299.
- Mayr M, Yusuf S, Weir G, Chung Y-L, Mayr U, et al. (2008) Combined metabolomic and proteomic analysis of human atrial fibrillation. *J Am Coll Cardiol* 51: 585–594.
- De Souza AI, Cardin S, Wait R, Chung Y-L, Vijayakumar M, et al. (2010) Proteomic and metabolomic analysis of atrial profibrillatory remodeling in congestive heart failure. *J Mol Cell Cardiol* 49: 851–863.
- Kourliouros A, Yin X, Didangelos A, Hossaini MT, Valencia O, et al. (2011) Substrate modifications precede the development of atrial fibrillation after cardiac surgery: a proteomic study. *Ann Thorac Surg* 92: 104–110.
- Picht E, DeSantiago J, Blatter LA, Bers DM (2006) Cardiac alternans do not rely on diastolic sarcoplasmic reticulum calcium content fluctuations. *Circ Res* 99: 740–748.
- Wang L, Myles RC, De Jesus NM, Ohlendorf AKP, Bers DM, et al. (2014) Optical mapping of sarcoplasmic reticulum Ca²⁺ in the intact heart: ryanodine receptor refractoriness during alternans and fibrillation. *Circ Res* 114: 1410–1421.
- Restrepo JG, Weiss JN, Karma A (2008) Calsequestrin-mediated mechanism for cellular calcium transient alternans. *Biophys J* 95: 3767–3789.
- Rovetti R, Cui X, Garfinkel A, Weiss JN, Qu Z (2010) Spark-induced sparks as a mechanism of intracellular calcium alternans in cardiac myocytes. *Circ Res* 106: 1582–1591.
- Alvarez-Lacalle E, Cantalapiedra IR, Peñaranda A, Cinca J, Hove-Madsen L, et al. (2013) Dependency of calcium alternans on ryanodine receptor refractoriness. *PLoS One* 8: e55042.
- Lugo CA, Cantalapiedra IR, Peñaranda A, Hove-Madsen L, Echebarria B (2014) Are SR Ca content fluctuations or SR refractoriness the key to atrial cardiac alternans?: insights from a human atrial model. *AJP Hear Circ Physiol* 306: H1540–H1552.
- Frisk M, Koivumäki JT, Norseng PA, Maleckar MM, Sejersted OM, et al. (2014) Variable t-tubule organization and Ca²⁺ homeostasis across the atria. *Am J Physiol Heart Circ Physiol* 307: H609–20.

55. Thul R, Coombes S, Roderick HL, Bootman MD (2012) Subcellular calcium dynamics in a whole-cell model of an atrial myocyte. *Proc Natl Acad Sci U S A* 109: 2150–2155.
56. Li Q, O'Neill SC, Tao T, Li Y, Eisner D, et al. (2012) Mechanisms by which Cytoplasmic Calcium Wave Propagation and Alternans Are Generated in Cardiac Atrial Myocytes Lacking T-Tubules—Insights from a Simulation Study. *Biophys J* 102: 1471–1482.
57. Koivumäki JT, Korhonen T, Tavi P (2011) Impact of sarcoplasmic reticulum calcium release on calcium dynamics and action potential morphology in human atrial myocytes: a computational study. *PLoS Comput Biol* 7: e1001067.
58. Voigt N, Heijman J, Wang Q, Chiang DY, Li N, et al. (2013) Cellular and Molecular Mechanisms of Atrial Arrhythmogenesis in Patients With Paroxysmal Atrial Fibrillation. *Circulation* 129: 145–156.
59. Harrild DM, Henriquez CS (2000) A Computer Model of Normal Conduction in the Human Atria. *Circ Res* 87: e25–36.
60. Krogh-Madsen T, Abbott GW, Christini DJ (2012) Effects of electrical and structural remodeling on atrial fibrillation maintenance: a simulation study. *PLoS Comput Biol* 8: e1002390.
61. McDowell KS, Vadakkumpadan F, Blake R, Blauer J, Plank G, et al. (2013) Mechanistic inquiry into the role of tissue remodeling in fibrotic lesions in human atrial fibrillation. *Biophys J* 104: 2764–2773.
62. Qu Z, Garfinkel A, Chen P-S, Weiss JN (2000) Mechanisms of Discordant Alternans and Induction of Reentry in Simulated Cardiac Tissue. *Circulation* 102: 1664–1670.
63. Defauw A, Kazbanov I V, Dierckx H, Dawyndt P, Panfilov A V (2013) Action potential duration heterogeneity of cardiac tissue can be evaluated from cell properties using Gaussian Green's function approach. *PLoS One* 8: e79607.
64. Jordan PN, Christini DJ (2007) Characterizing the contribution of voltage- and calcium-dependent coupling to action potential stability: implications for repolarization alternans. *Am J Physiol Heart Circ Physiol* 293: H2109–18.
65. Krummen DE, Narayan SM (2009) Mechanisms for the initiation of human atrial fibrillation. *Heart Rhythm* 6: S12–6.
66. Krummen DE, Bayer JD, Ho J, Ho G, Smetak MR, et al. (2012) Mechanisms for Human Atrial Fibrillation Initiation: Clinical and Computational Studies of Repolarization Restitution and Activation Latency. *Circ Arrhythm Electrophysiol* 5: 1149–1159.
67. Dössel O, Krueger MW, Weber FM, Wilhelms M, Seemann G (2012) Computational modeling of the human atrial anatomy and electrophysiology. *Med Biol Eng Comput* 50: 773–799.
68. Shiferaw Y, Watanabe MA, Garfinkel A, Weiss JN, Karma A (2003) Model of intracellular calcium cycling in ventricular myocytes. *Biophys J* 85: 3666–3686.
69. Vigmond EJ, Hughes M, Plank G, Leon LJ (2003) Computational tools for modeling electrical activity in cardiac tissue. *J Electrocardiol* 36: 69–74.
70. Plank G, Zhou L, Greenstein JL, Cortassa S, Winslow RL, et al. (2008) From mitochondrial ion channels to arrhythmias in the heart: computational techniques to bridge the spatio-temporal scales. *Philos Trans R Soc Ser A Math Phys Eng Sci* 366: 3381–3409.
71. Vigmond EJ, Weber dos Santos R, Prassl AJ, Deo M, Plank G (2008) Solvers for the cardiac bidomain equations. *Prog Biophys Mol Biol* 96: 3–18.